Supporting information

Controlling the C_1/C_{2+} product selectivity of electrochemical CO_2 reduction upon tuning bimetallic CuIn electrocatalyst composition and operating conditions

Lin Gu[a], Abhishek Dutta Chowdhury[a],*

[a] *College of Chemistry and Molecular Sciences, Wuhan University, Wuhan, Hubei 430072, P. R. China*

* Corresponding author

E-mail address: abhishek@whu.edu.cn

Experimental Section

Materials and reagents

All chemicals were used as purchased without further purification. Copper (II) nitrate trihydrate $Cu(NO_3)_2 \cdot 3H_2O$, indium (III) nitrate hydrate $In(NO_3)_3 \cdot xH_2O$, and potassium bicarbonate ($KHCO_3$) were obtained from Innochem (Beijing) Science & Technology Co., Ltd (Beijing, China). Sodium carbonate (Na_2CO_3) was purchased from Bidepharm Co. Ltd (Shanghai, China). Nafion solution (5 %) was purchased from Dupont China Holding Co. Ltd. Potassium hydroxide (KOH) was purchased from Sinopharm Chemical Reagent Co. Ltd (Shanghai, China). High-purity CO_2 (≥99.99%) and Ar (≥99.99%) was supplied by Zxrygas Co. Ltd (Wuhan, China).

Characterization

X-ray diffraction (XRD) was performed using a Rigaku Smartlab SE system with Cu Kα radiation in the 2θ range from 5° to 90°. X-ray photoelectron spectroscopy (XPS) was performed using a Thermo ESCALAB 250Xi spectrometer, with a monochromated Al-Kα (1486.6 eV). Scanning electron microscopy (SEM) and transmission electron microscopy (TEM) were performed on a scanning microscope (Hitachi S4800 field-emission) operated at 15 kV and a transmission electron microscope (Tecnai G2 F30 S-TWIN), respectively. The TEM samples were prepared by dispersing catalyst powder in alcohol by ultra-sonication, and a droplet of this ink was dropped onto TEM grids with carbon film. The copper and indium content was determined by inductively coupled plasma optical emission spectroscopy (ICP-OES) analysis using the emission spectrometer (Agilent ICPOES730).

The crystallite size of $InCu_nO_x$ was calculated using the Scherrer's equation[1]:

$$D = \frac{K\lambda}{Bcos\theta}$$

Where k is the configuration component (0.9), λ is the wavelength of X-ray radiation, θ is Bragg's intersection of the prominent and B is angular broadness of peaks at full width at half maximum (FWHM)[1].

Materials synthesis of $InCu_nO_x$

The $InCu_nO_x$-based materials were prepared by the co-precipitation-calcination method. 3.3/0.7 mmol of $In(NO_3)_3 \cdot xH_2O$ and 0.35/0.7/2.5/4.1 mmol of $Cu(NO_3)_2 \cdot 3H_2O$ were dissolved in deionized water (14.3 mL). 94 mmol of Na_2CO_3 was also dissolved in deionized water (100 mL) to form a transparent solution and added dropwise to the above metallic solution under stirring at room temperature to reach a pH of 9.2. Then, the bimetallic precipitate was recovered by centrifugation and dried in a vacuum oven (60 °C). These materials were then calcined for 3 h at 300 °C (2 °C min^{-1}) in the static air, which led to the electrocatalysts of composition $InCu_nO_x$. Herein, these catalytic materials were named based on the different content of Cu (i.e., n as identified by ICP-OES, see Table S1), where n = 5, 10, 25, and 73 were synthesized by using a similar strategy by adjusting the concentration of $In(NO_3)_3 \cdot xH_2O$ and $Cu(NO_3)_2 \cdot 3H_2O$.

Preparation of electrodes for eCO_2R in H-type cell and flow cell

1 mg of $InCu_nO_x$ powder was dispersed into a solution containing 500 μL isopropanol, and 500 μL deionized water, and 40 μL of nafion solution (5%); subsequently, the ink was dropped onto carbon paper (1 cm × 1 cm). The $InCu_nO_x$ materials were uniformly loaded on carbon paper and acted as the working electrode (1 mg cm^{-2}).

Electrochemical measurements

All electrochemical measurements were assessed using a CHI 760E electrochemical workstation with an H-type cell (Gaossunion, China) and flow cell (Dioxide Materials, America). The H-type cell experiments were carried out in a gas-tight two-compartment H-type cell separated by a Nafion-117 membrane under ambient conditions. Ag/AgCl electrode and Pt sheet electrode were used as the reference and counter electrode, respectively. CO_2-saturated 0.1 M $KHCO_3$ was used as the electrolyte for the H-type cell (anode and cathode chambers). Flow cell studies were performed using a gas diffusion electrode (GDE) flow cell, including a Ti current collector with interdigitated gas-diffusion channels, a 3D printed chamber with ports for electrolyte flow and reference electrode, and a Ni foam inserted in a pocket of Ti current collector as the anode. Anion exchange membrane (Fumasep FAA-3-PK-130) and cation exchange membrane (Nagfion-117) were used to separate the cathode and anode chambers. A leak-free Ag/AgCl electrode was used as the reference electrode. The above-prepared electrodes were used as working electrodes with an effective area of 1 cm^2. The catholyte and anolyte were each 30 mL of 1 M KOH/0.1 M $KHCO_3$ solution circulated using peristaltic pumps (Rongbaipump, China) at a flow rate of 5 mL min^{-1}. For both H-type cell and flow cell studies, CO_2 gas flow was controlled by a mass flow controller at a specified flow rate of 20 sccm, and the applied potentials were iR-compensated and converted to the RHE scale. All the potentials in this work were converted to the reversible hydrogen electrode (RHE) according to the formula:

$$E\ (RHE) = E\ (Ag/AgCl) + 0.197 + 0.059 \times pH.$$

The reported partial current densities for eCO_2R were normalized to geometric surface

areas. Electrochemical impedance spectroscopy (EIS) and electrochemical surface area (ECSA) measurements were measured under CO_2-saturated electrolyte.

Electrochemical CO_2 reduction experiments

Electrochemical CO_2 reduction (eCO₂R) was conducted in a CO_2-saturated electrolyte. The chronoamperometry was performed at the potential range from −0.8 V to −1.2 V *vs.* RHE for the 0.1 M $KHCO_3$ and −0.5 V to −1 V *vs.* RHE for 1 M KOH. The gas-phase products were analyzed by an online gas chromatograph (GC, Ruimin, China). The thermal conductivity detector (TCD) was used for H_2 analysis, and the flame ionization detector (FID) was used for CO (with a methanizer), CH_4, and C_2H_4 analysis. The faradaic efficiency for gas- and liquid-phase products were calculated by using $FE = \dfrac{nFCivP}{jRT}$ and $FE = \dfrac{nFCiV}{Q}$, respectively, where n is the number of electrons transferred for electrochemical reduction of CO_2 to each target product molecule, F is the Faraday constant (96485 C mol^{-1}), Ci is the concentration of the target product analyzed by GC or NMR (Bruker AVANCE III 600), v is the inlet gas flow rate (20 sccm), j is current. T, P, and R are the temperature, the pressure, and the gas constant, respectively. V is the volume of the cathode electrolyte, and Q is the total charge during the eCO₂R. CO_2 electrolysis was performed under various operating conditions and tested twice independently. The error bars represent standard deviation of two independent measurements conducted under the same conditions. The post-reacted $InCu_5O_x$ and $InCu_{73}O_x$ electrocatalysts after eCO₂R were prepared for the characterization (TEM and XPS) using a flow cell at an applied potential of −0.8 V vs. RHE for 1 h (with AEM) and an H-type cell at an applied potential of −1.2 V vs. RHE for 1 h (with CEM).
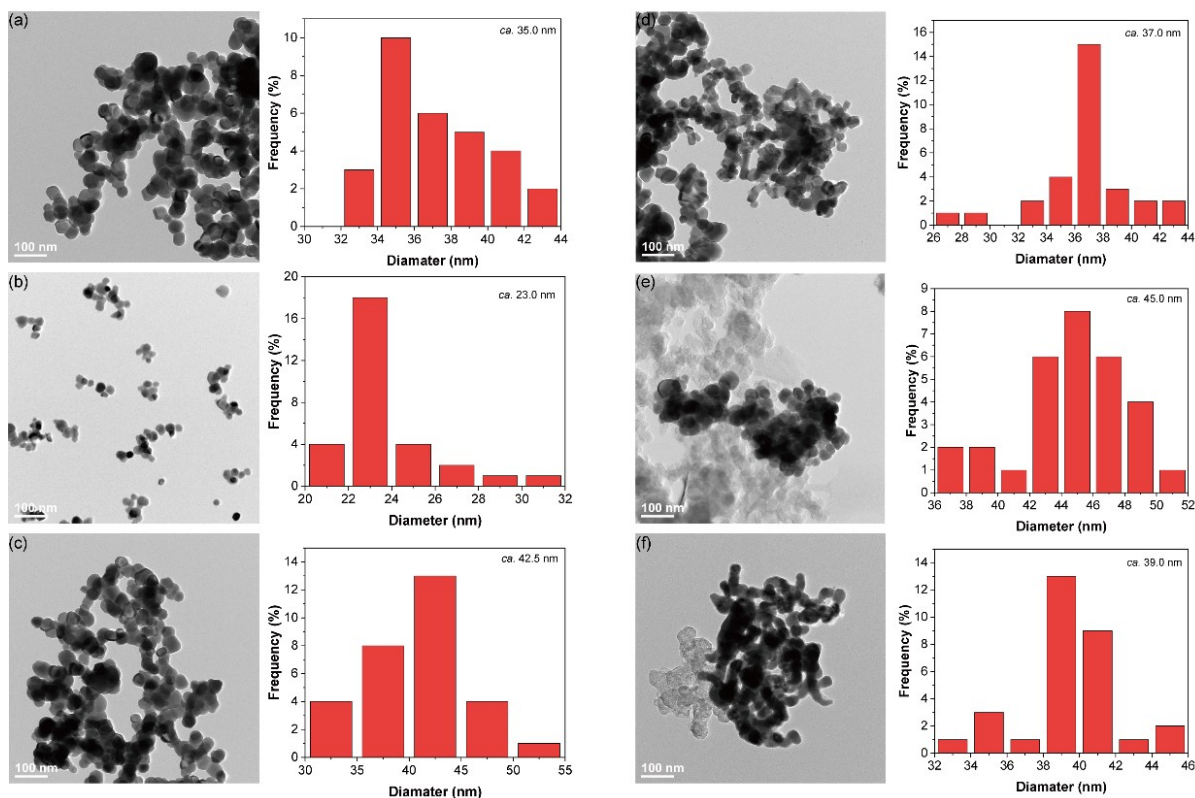
Fig. S1. (a) TEM images of as-synthesized $InCu_5O_x$ material with an average diameter of 35.0 nm. (b) TEM images of as-synthesized $InCu_{10}O_x$ material with an average diameter of 23.0 nm. (c) TEM images of as-synthesized $InCu_{25}O_x$ material with an average diameter of 42.5 nm. (d) TEM images of as-synthesized $InCu_{73}O_x$ material with an average diameter of 37.0 nm. (e) TEM images of post-reacted $InCu_5O_x$ material after eCO$_2$R in a flow cell (-0.8 V *vs.* RHE for 1 h) with an average diameter of 45.0 nm. (f) TEM images of post-reacted $InCu_{73}O_x$ material after eCO$_2$R in a flow cell (-0.8 V *vs.* RHE for 1 h) with an average diameter of 39.0 nm.
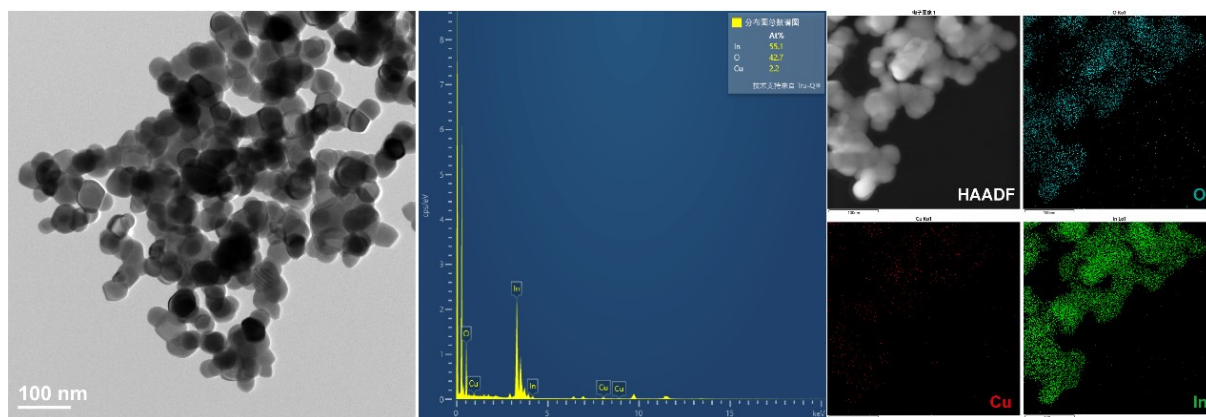
Fig. S2. EDX spectrum and elemental mappings show uniform nanoparticle morphology, where the Cu, In, and O elements are evenly distributed over the InCu$_5$O$_x$ material.
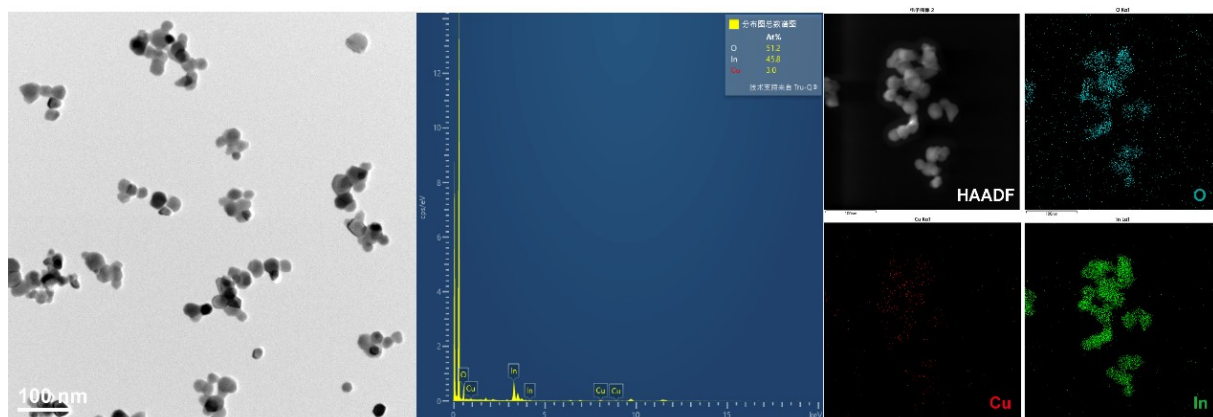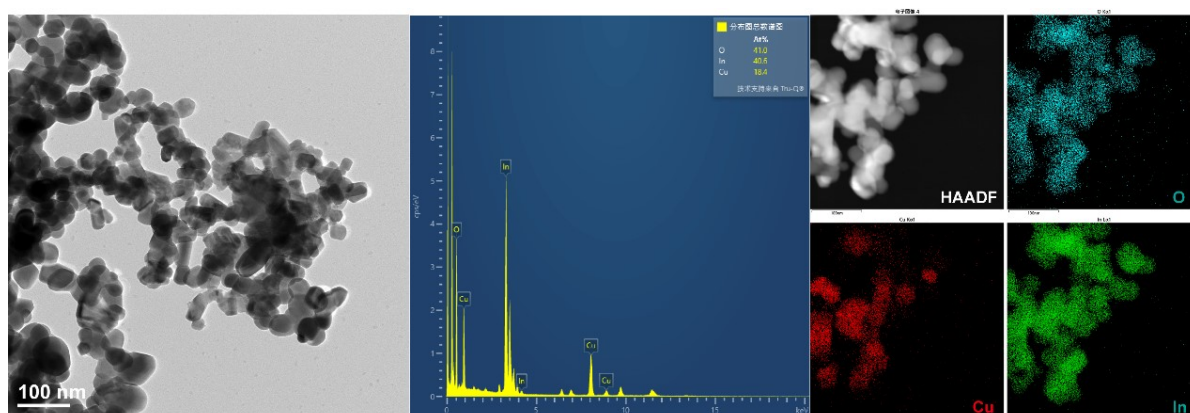
Fig. S3. EDX spectrum and elemental mappings show uniform nanoparticle morphology, where the Cu, In, and O elements are evenly distributed over the $InCu_{10}O_x$ material.
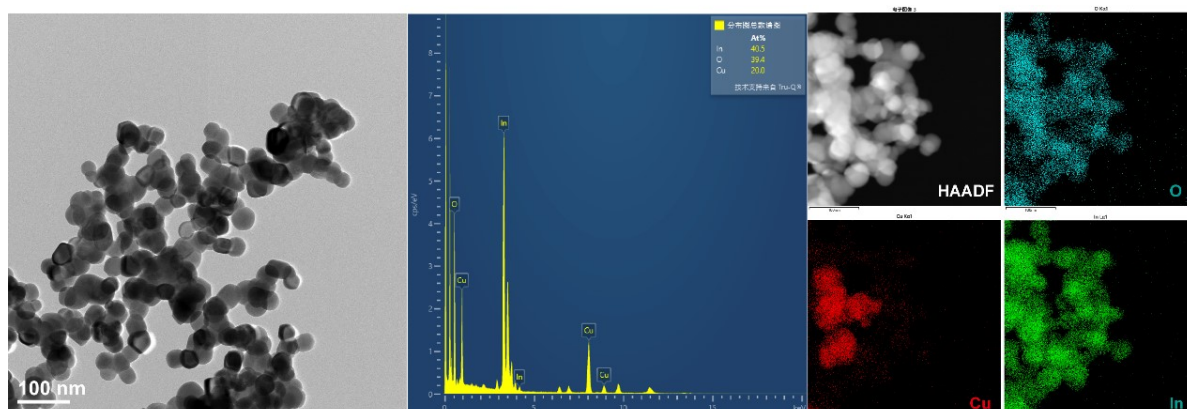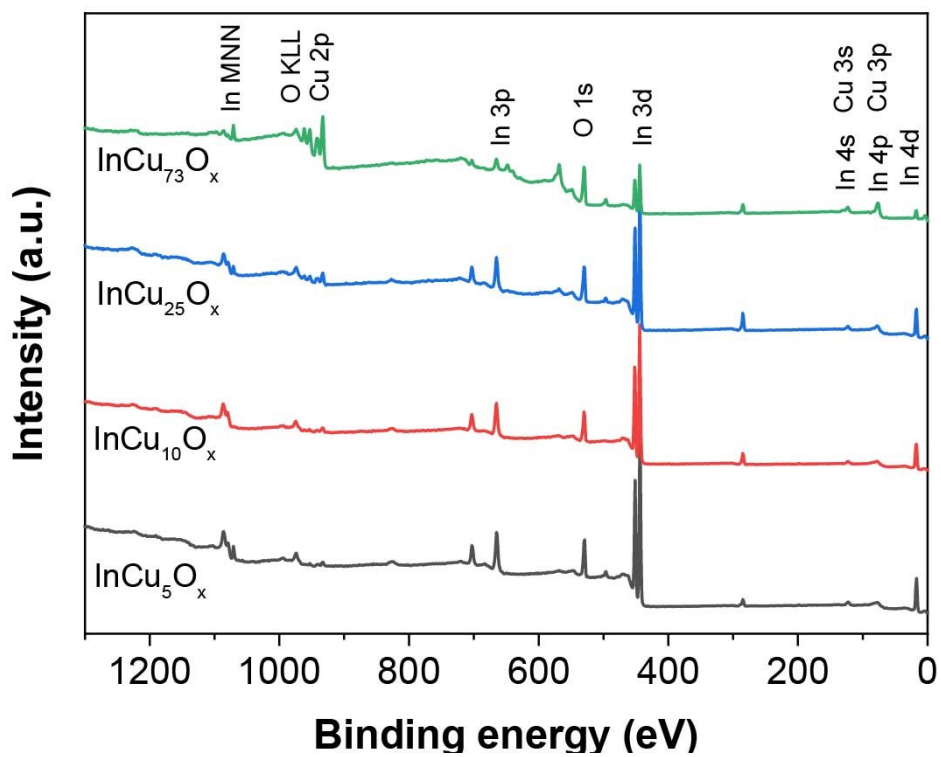
Fig. S4. EDX spectrum and elemental mappings show uniform interconnected nanoparticle morphology, where the Cu, In, and O elements are evenly distributed over the $InCu_{25}O_x$ material.

Fig. S5. EDX spectrum and elemental mappings show uniform interconnected nanoparticle morphology, where the Cu, In, and O elements are evenly distributed over the $InCu_{73}O_x$ material.

Fig. S6. XPS survey scan of InCu$_n$O$_x$ materials comprising Cu 2p, In 3d, O 1s, and Cu LMM

spectra.
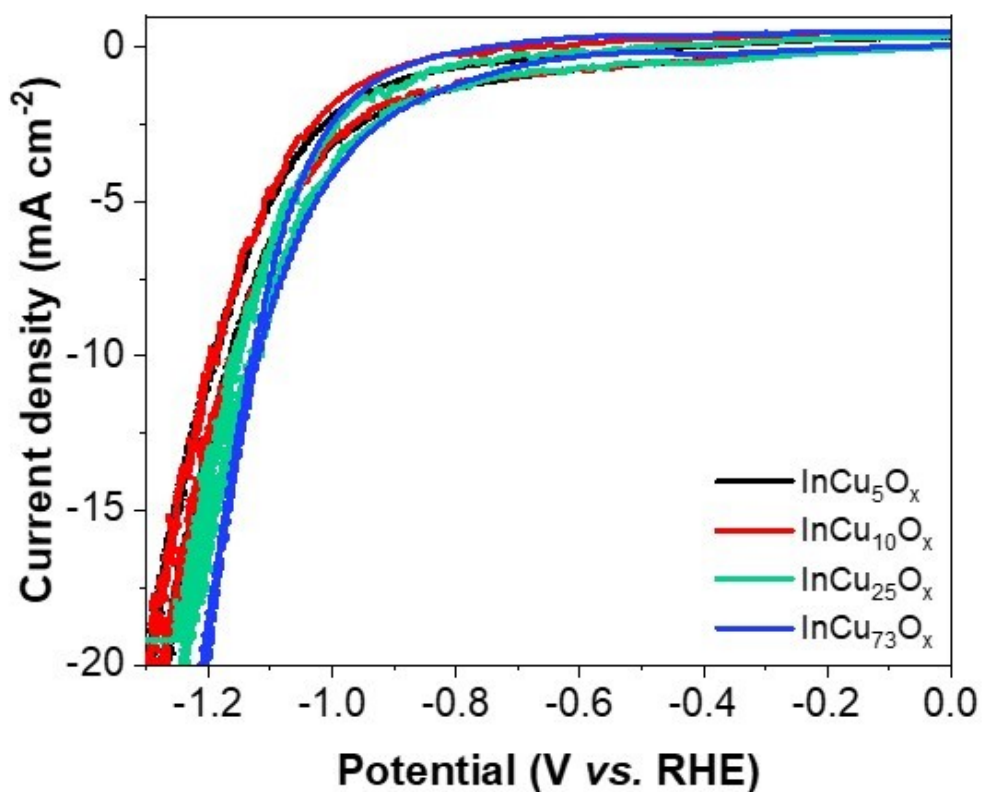
Fig. S7. To stabilize the $InCu_nO_x$ electrode surface, cyclic voltammetry (CV) measurements were performed before the eCO_2R reaction. Herein, CV curves for $InCu_nO_x$ materials were measured in CO_2-saturated 0.1 M $KHCO_3$ electrolyte (pH = 6.8) using an H-type cell (CEM) with a sweeping rate of 10 mV s^{-1} from 0 to -1.3 V versus the reversible hydrogen electrode (*vs.* RHE).
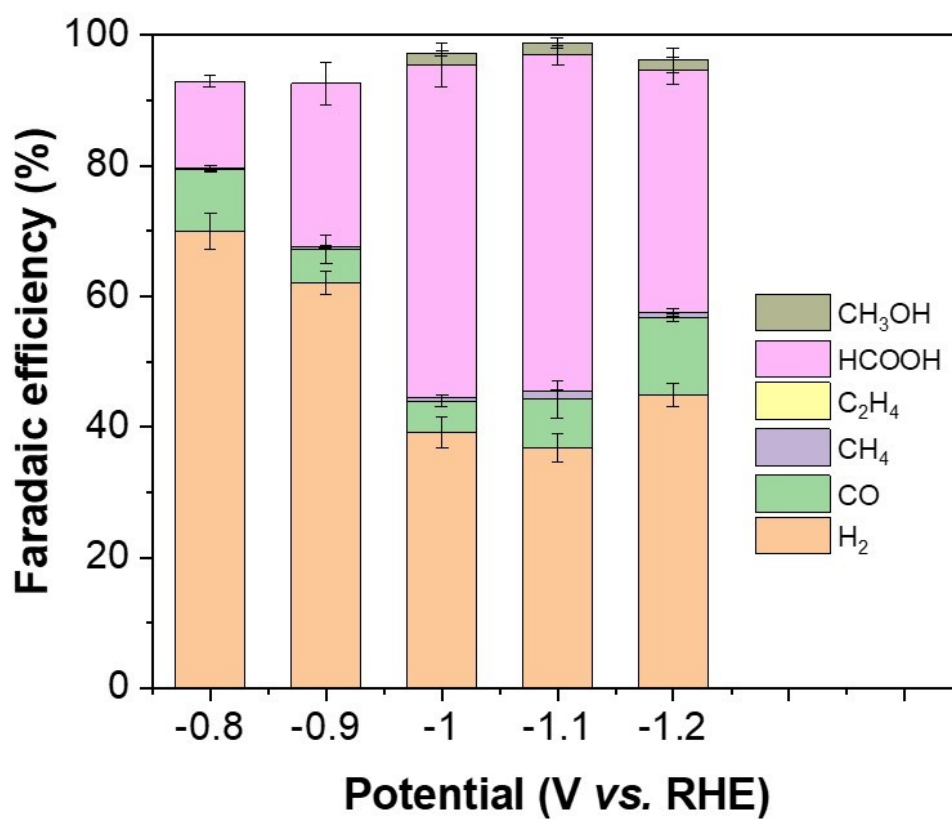
Fig. S8. The FE for different eCO$_2$R products at selected potentials over InCu$_{10}$O$_x$ materials in CO$_2$-saturated 0.1 M KHCO$_3$ using H-type cell with CEM. See Fig. 5c for the comparable data over InCu$_{73}$O$_x$ material.
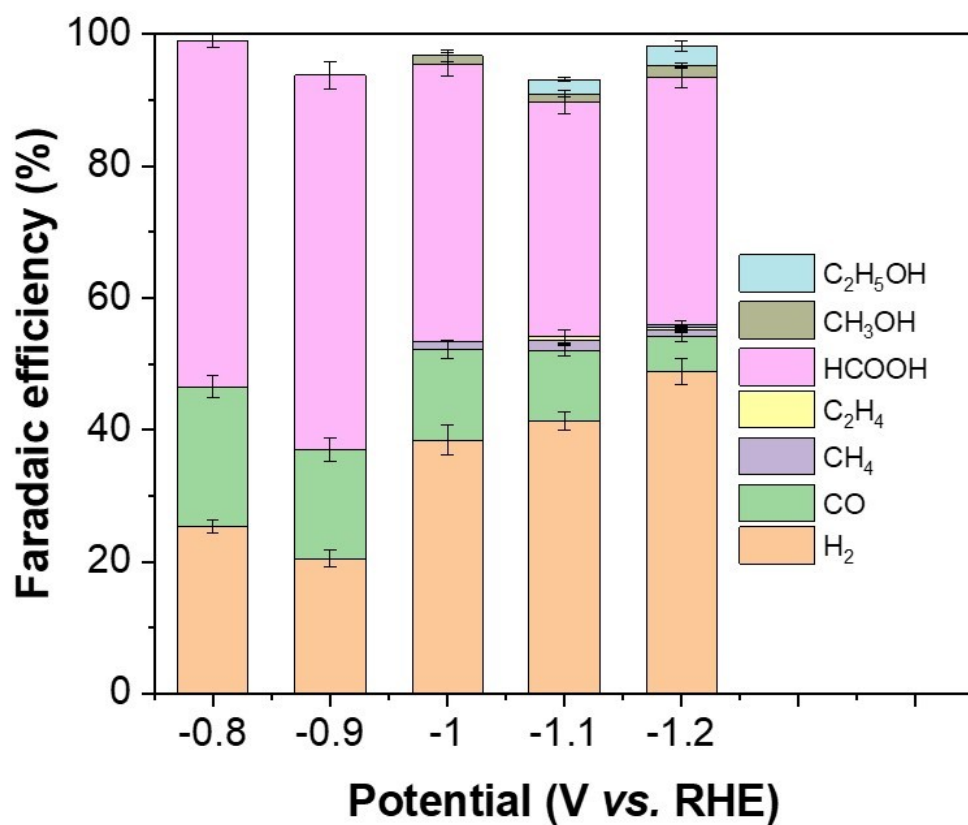
Fig. S9. The FE for different eCO$_2$R products at selected potentials over InCu$_{25}$O$_x$ material in CO$_2$-saturated 0.1 M KHCO$_3$ using H-type cell with CEM. See Fig. 5c for the comparable data over InCu$_{73}$O$_x$ material.
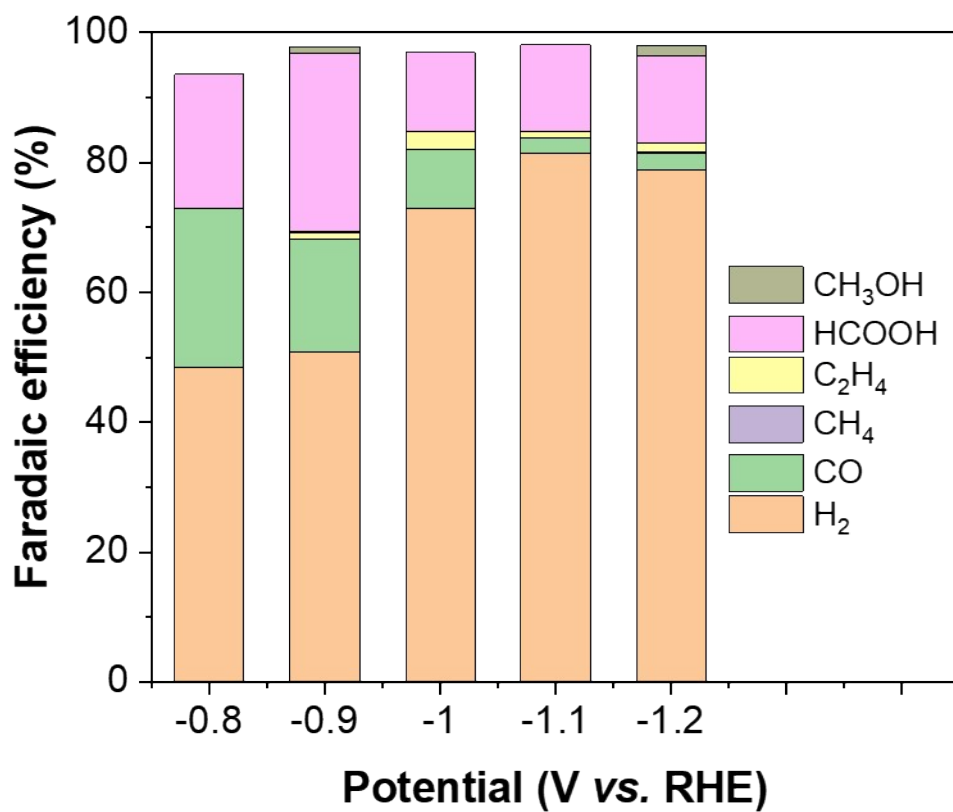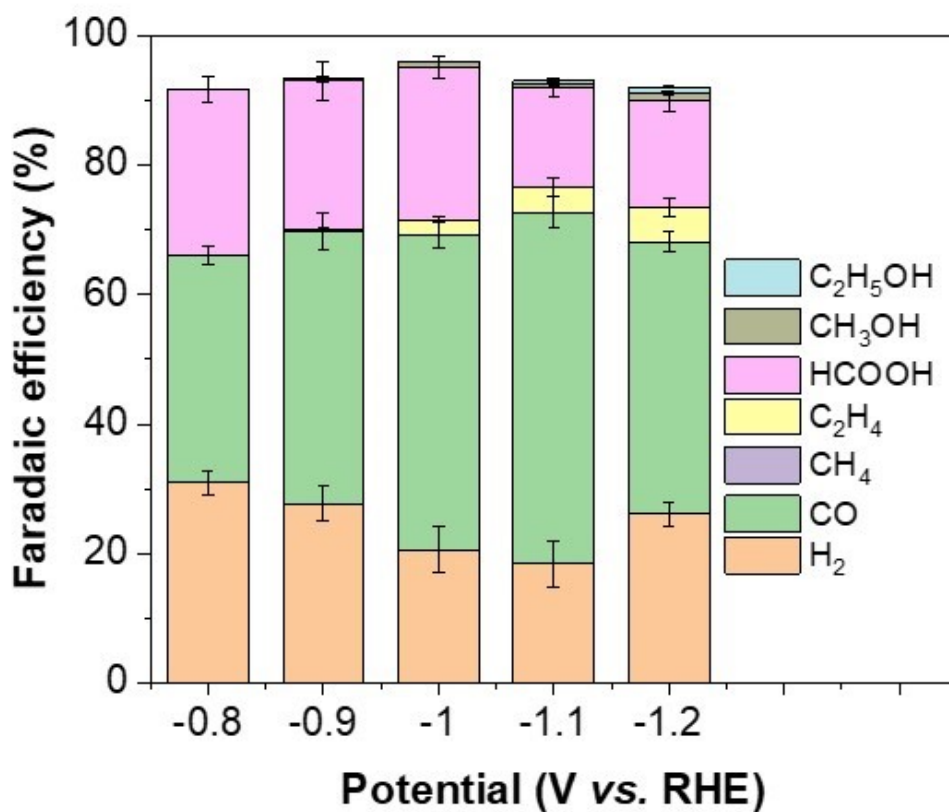
Fig. S10. The FE for different eCO$_2$R products at selected potentials over InCu$_{73}$O$_x$ material in CO$_2$-saturated 0.5 M KHCO$_3$ using H-type cell with CEM. See Fig. 5c for the comparable data over InCu$_{73}$O$_x$ material (0.1 M KHCO$_3$).
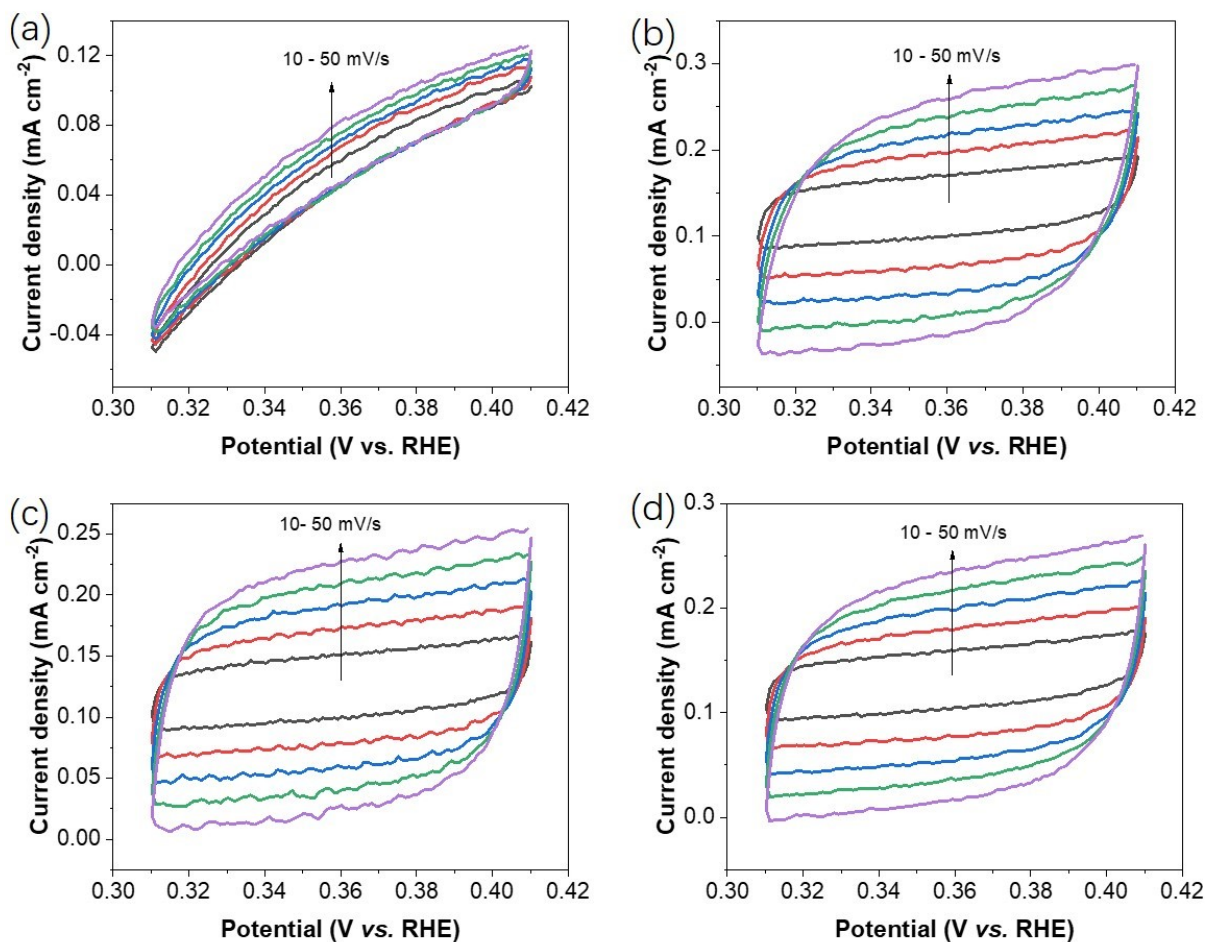
Fig. S11. CV was performed at scan rates of 10 mV s^{-1}, 20 mV s^{-1}, 30 mV s^{-1}, 40 mV s^{-1}, and 50 mV s^{-1} in a CO_2-bubbled 0.1 M $KHCO_3$ electrolyte (H-type cell with CEM) for (a) $InCu_5O_x$, (b) $InCu_{10}O_x$, (c) $InCu_{25}O_x$, and (d) $InCu_{73}O_x$ materials. The potential window of the CV curve was selected between 0.31 V and 0.41 V *vs.* RHE (double-layer charging and discharging interval).

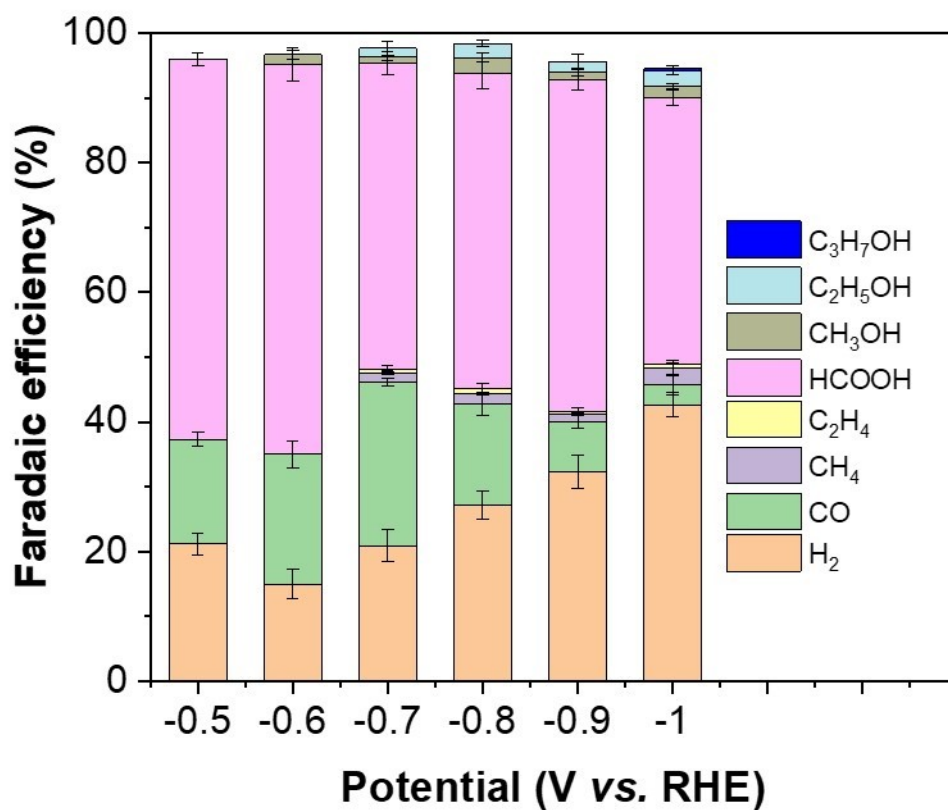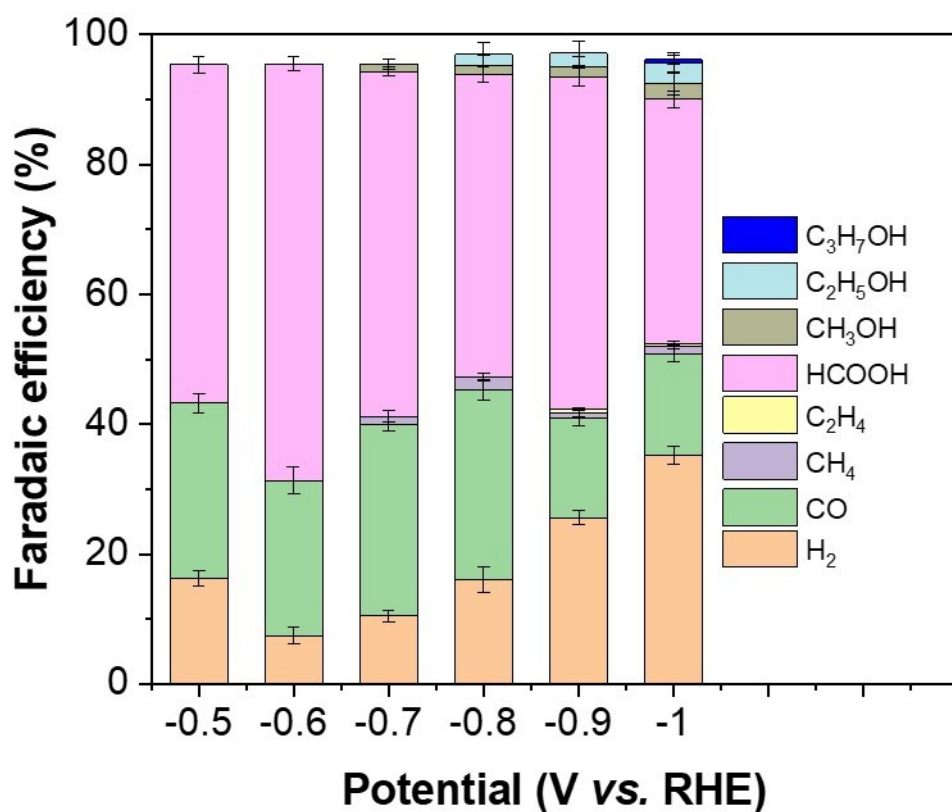**Fig. S12.** The FE for different eCO$_2$R products at selected potentials over InCu$_{73}$O$_x$ material in a flow cell with CEM (0.1 M KHCO$_3$). See Fig. 7c for the comparable data over InCu$_{73}$O$_x$ material (in 1 M KOH using flow cell with AEM).
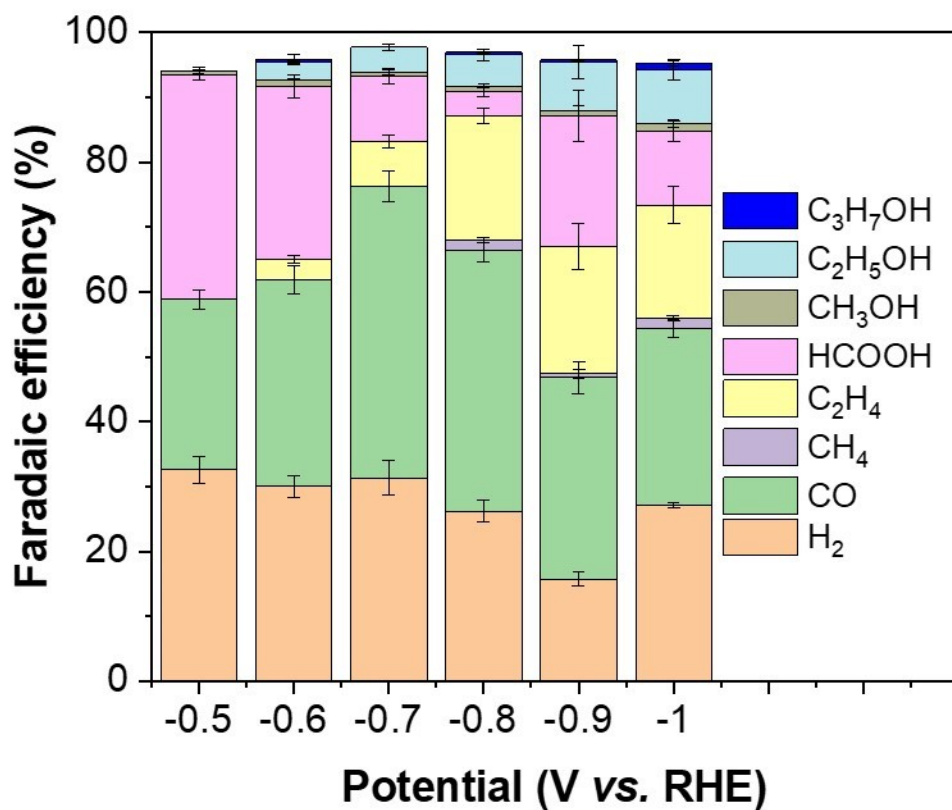
Fig. S13. FE for different products at selected potentials in CO_2-saturated 1 M KOH using a flow cell with CEM: $InCu_{73}O_x$. Six primary eCO_2R products were obtained (i.e., CO, CH_4, HCOOH, CH_3OH, C_2H_4, C_2H_5OH, and C_3H_7OH) along with HER-liberated H_2. See Fig. 7c for the comparable data over $InCu_{73}O_x$ material (with AEM).
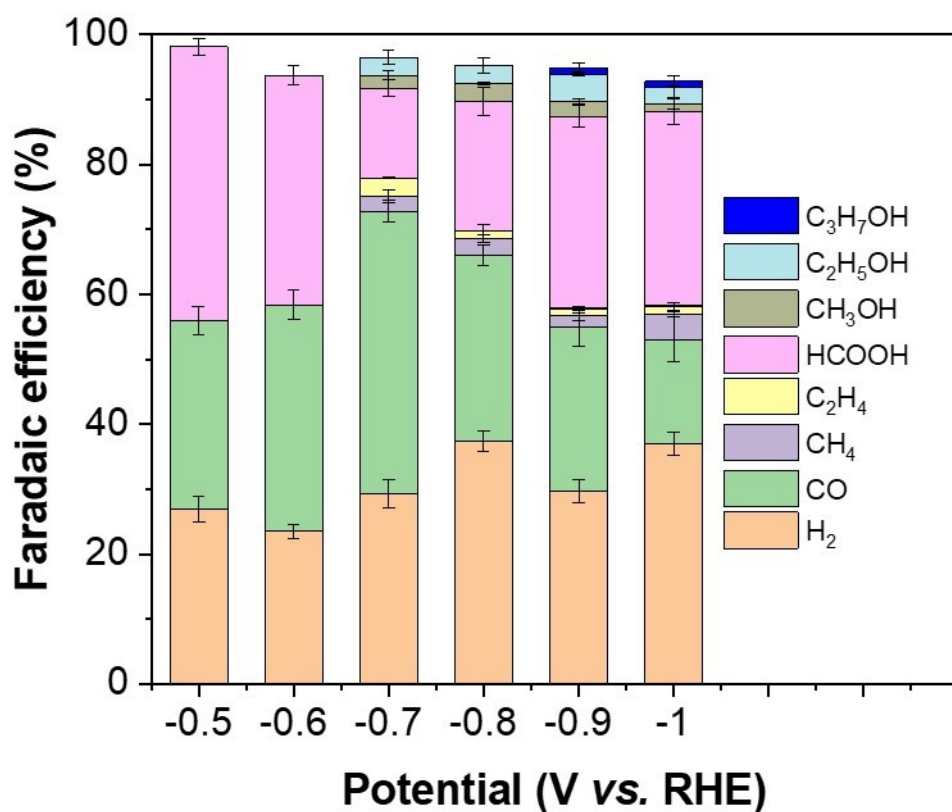
Fig. S14. FE for different products at selected potentials in CO_2-saturated 1 M KOH using a flow cell with AEM: $InCu_5O_x$. Six primary eCO_2R products were obtained (i.e., CO, CH_4, HCOOH, CH_3OH, C_2H_4, C_2H_5OH, and C_3H_7OH) along with HER-liberated H_2. See Fig. 7c for the comparable data over $InCu_{73}O_x$ material.

Fig. S15. FE for different products at selected potentials in CO_2-saturated 1 M KOH using a flow cell with AEM: $InCu_{10}O_x$. Six primary eCO_2R products were obtained (i.e., CO, CH_4, HCOOH, CH_3OH, C_2H_4, C_2H_5OH, and C_3H_7OH) along with HER-liberated H_2. See Fig. 7c for the comparable data over $InCu_{73}O_x$ material.
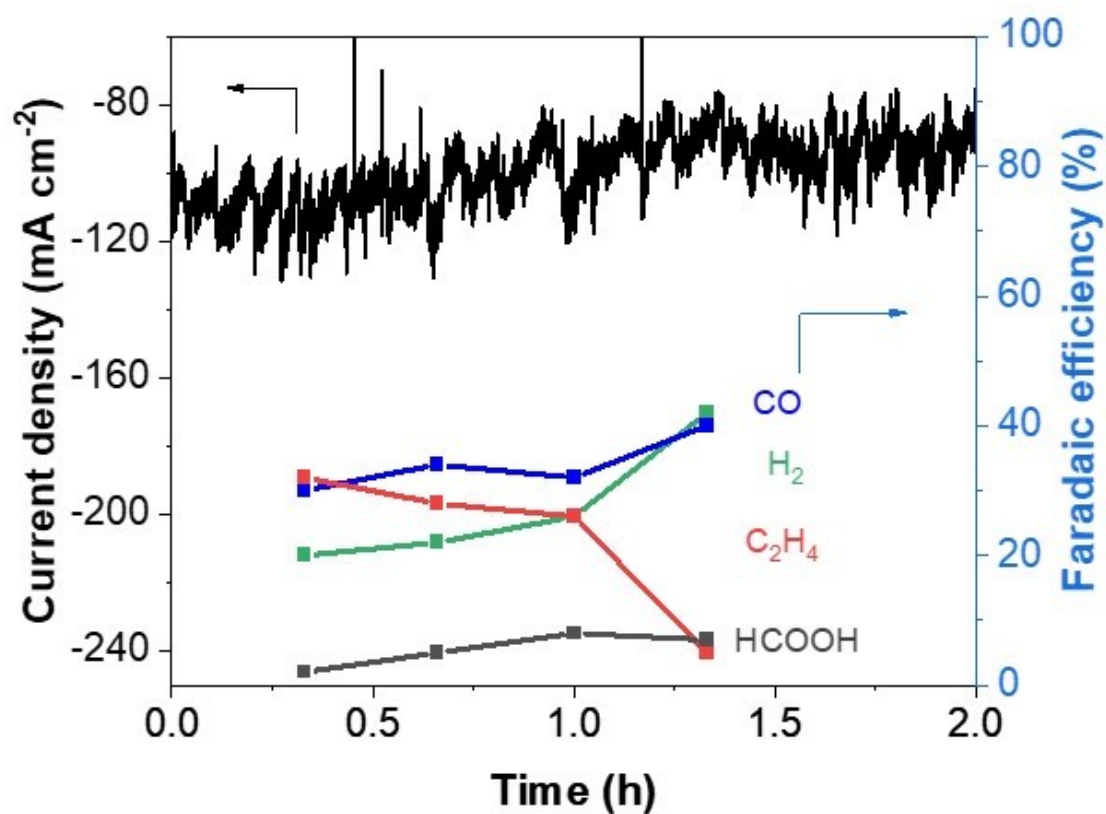
Fig. S16. FE for different products at selected potentials in CO_2-saturated 1 M KOH using a flow cell with AEM: $InCu_{25}O_x$. Six primary eCO_2R products were obtained (i.e., CO, CH_4, HCOOH, CH_3OH, C_2H_4, C_2H_5OH, and C_3H_7OH) along with HER-liberated H_2. See Fig. 7c for the comparable data over $InCu_{73}O_x$ material.

Fig. S17. Evaluation of eCO$_2$R electrocatalytic performance in the flow cell system with AEM (1 M KOH): Stability testing of InCu$_{73}$O$_x$ catalyst for 2 h. Left y-axis: current density of the InCu$_{73}$O$_x$ at −0.8 V vs. RHE. Right y-axis: the FE$_{H2}$, FE$_{CO}$, FE$_{HCOOH}$, and FE$_{C2H4}$.
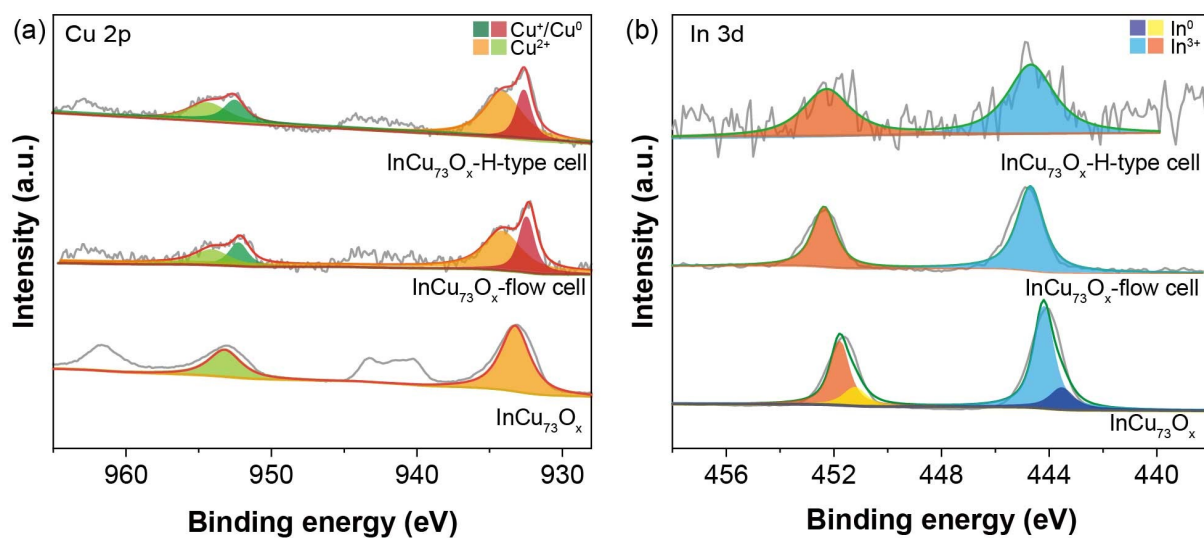
Fig. S18. Summary of XPS characterization: (a) Cu 2p spectra of $InCu_{73}O_x$ before and after eCO_2R in a flow cell with AEM (−0.8 V vs. RHE for 1 h) and H-type cell with CEM (−1.2 V vs. RHE for 1 h). (b) In 3d spectra of $InCu_{73}O_x$ before and after eCO_2R in a flow cell with AEM (−0.8 V vs. RHE for 1 h) and H-type cell with CEM (−1.2 V vs. RHE for 1 h).

Table S1. The atom percentage of different elements in as-synthesized catalysts

Sample	Cu loading (wt%) [a]	In loading (wt%) [a]
$InCu_5O_x$	5.27	74.06
$InCu_{10}O_x$	10.05	71.24
$InCu_{25}O_x$	25.18	51.61
$InCu_{73}O_x$	73.48	5.34

[a] Estimated by ICP-OES. Since this work focuses on Cu-part of the catalyst, its ICP loading was reflected in their corresponding names.

Table S2. Main textural parameters of $InCu_5O_x$, $InCu_{10}O_x$, $InCu_{25}O_x$ and $InCu_{73}O_x$.

catalyst	XPS (at%)					EDS (at%)			crystallite Size (nm) (-111) Facet of CuO
	Cu^{2+} [a]	Cu^+ [a]	Cu [b]	In [b]	O [b]	Cu	In	O	
$InCu_5O_x$	69.15	30.85	5.46	32.12	62.41	2.67	23.33	73.99	26.12
$InCu_{10}O_x$	77.40	22.60	7.02	31.09	61.89	6.89	30.15	62.97	20.17
$InCu_{25}O_x$	82.31	17.69	12.64	25.00	62.36	8.27	30.44	61.29	21.73
$InCu_{73}O_x$	100	0	41.88	6.96	51.16	30.70	2.93	66.37	21.16

[a] Calculated by the XPS quantitative analysis using the narrow spectra (Cu 2p).

[b] Calculated by the XPS survey scans.

Table S3. Catalytic performance of reported bimetallic CuIn-based catalysts in literature.

Samples	E (V) *vs.* RHE	Cell-type	electrolyte	Main product	FE of main product (%)	Ref.
CuIn alloy nanowires	-1	H-type cell	0.1 M KHCO$_3$	CO	86	[2]
Cu-In electrode	-0.6	H-type cell	0.1 M KHCO$_3$	CO	40	[3]
Cu-In$_2$O$_3$/C	-0.7	H-type cell	0.1 M KHCO$_3$	CO	95	[4]
CuIn-30		H-type cell	0.1 M KHCO$_3$	formate	87.4	[5]
Cu-In hybrid	-0.59	H-type cell	0.1 M KHCO$_3$	CO	75.8	[6]
In$_{1.5}$Cu$_{0.5}$ nanoparticles	-1.2	H-type cell	0.1 M KHCO$_3$	CO	90	[7]
dendritic copper-indium	-1	H-type cell	0.1 M KHCO$_3$	formate	80	[8]
InCu$_n$O$_x$	-0.8	H-type cell	0.1 M KHCO3	CO	51	This work
InCu$_n$O$_x$	-0.8	Flow cell	1 M KOH	C$_{2+}$(C$_2$H$_4$+C$_2$H$_5$OH+C$_3$H$_7$OH)	37	This work

References

1   S. U. Din, M. Sajid, M. Imran, J. Iqbal, B. A. Shah, M. Azeem Ullah and S. Shah, *Mater. Res. Express*, 2019, **6**, 085022.

2   Q. Zhou, X. Tang, S. Qiu, L. Wang, L. Hao and Y. Yu, *Mater. Today Phys.*, 2023, **33**, 101050.

3   S. Rasul, D. H. Anjum, A. Jedidi, Y. Minenkov, L. Cavallo and K. Takanabe, *Angew. Chemie*, 2015, **127**, 2174–2178.

4   Y. Jia, H. S. Hsu, W. C. Huang, D. W. Lee, S. W. Lee, T. Y. Chen, L. Zhou, J. H. Wang, K. W. Wang and S. Dai, *Nano Lett.*, 2023, **23**, 2262–2268.

5   J. Shao, Y. Wang, D. Gao, K. Ye, Q. Wang and G. Wang, *Chinese J. Catal.*, 2020, **41**, 1393–1400.

6   Q. Xie, G. O. Larrazábal, M. Ma, I. Chorkendorff, B. Seger and J. Luo, *J. Energy Chem.*, 2021, **63**, 278–284.

7   B. Wei, Y. Xiong, Z. Zhang, J. Hao, L. Li and W. Shi, *Appl. Catal. B Environ.*, 2021, **283**, 119646.

8   Z. B. Hoffman, T. S. Gray, K. B. Moraveck, T. B. Gunnoe and G. Zangari, *ACS Catal.*, 2017, **7**, 5381–5390.